International Journal of Control, Automation, and Systems 22(1) (2024) 265-275
http://dx.doi.org/10.1007/s12555-022-0966-y
ISSN:1598-6446 eISSN:2005-4092
http://www.springer.com/12555

Comparative Performance Analysis of AC Magnetic Positioning Algorithms With Realtime Implementation Environment

Byungjin Lee , Juhwan Lee , and Sangkyung Sung*

Abstract: This study proposes an enhanced algorithm design and comparative performance analysis of the positioning system based on the concurrent AC magnetic fields. For this, a new approximated field representation model with respect to the circular magnetic coil is developed for achieving on-board algorithm implementation. In the existing researches, the magnetic positioning is usually implemented by the dipole model even though they employ circular coils. Despite the model simplicity, the dipole model suffers typically from the significant representation model deviation from actual magnetic measurement near the transmitter coil area. To overcome this, more complicated but computationally comparable formula is employed, which can reflect effectively the dimensional field distribution characteristics of the magnetic coil. This study also investigates a real-time implementation of the proposed method. Considering the computing performance of the microprocessor, the on-board algorithm is developed considering its calculation speed and memory usage. As a result, the real-time result achieved millimeters level difference compared with the post processing result using full computing power. In experimental validation, a reference optical positioning system providing a sub-millimeter accuracy is employed for evaluating the on-board real-time results during dynamic trajectory tests. The result presents an enhanced estimation error around full operational range compared with the other representation models, which specifically demonstrates centimeters level error in positioning and about 3 degree heading error within operation range.

Keywords: AC magnetic fields, magnetic positioning, on board unit, real-time system, system implementation.

1. INTRODUCTION

The electromagnetic signal, including light, usually has a straightness radiation characteristic. This allows the signal to travel further, and its attenuation in space is well expected by a simple geometric equation. These characteristics are useful for ToF (time of flight) or RSS (received signal strength) technique as navigation methods. However, the attenuation of the electromagnetic signal is drastically changed by the kinds of the medium between transmitter and receiver. This problem causes performance degradation or a failure, so almost all methods using electromagnetic wave as a primary means of navigation necessitate sensors' LOS (line of sight). Keeping the LOS is a major constraint of the navigation methods like UWB positioning, satellite navigation systems, vision or lidar odometry.

The magnetic signal with high frequency wave may also affect many kinds of materials, and MRI (magnetic resonance image) is one of the examples of the usage. But the permeability of magnetic signal is intrinsically excellent in comparison with the electromagnetic one. Compared with other radio-based robotic localization methods, it is known magnetic positioning has robustness to measurement variation caused by the surrounding medium. This is because a magnetic field intrinsically demonstrates excellent permeability through the magnetic flux path except for ferromagnetic obstacles and has the advantage that the magnetic attenuation effect is negligible for most environmental objects, e.g., air, water, organic body, wood, concrete, plastics, etc. Therefore, studies using the artificially generated magnetic field signals for indoor localization, robotics underwater or inside the human body have been widely published in recent days [1-4].

Unlike the electromagnetic one, the magnetic field exists as dipole and these two poles cancel each signal strength. This dipole constrain causes the short coverage of the magnetic field by coils or magnets, so the navigation area is inevitably limited. By increasing the current in

Manuscript received October 20, 2022; revised April 4, 2023; accepted June 3, 2023. Recommended by Associate Editor Jong-Han Kim under the direction of Senior Editor Hyun Myung. This research was supported by the Sejong Fellowship Program (NRF-2022R1C1C2009014), the Basic Research Program (NRF-2022R1A2C1005237), and the Unmanned Vehicles Core Technology Research and Development Program (NRF-2020M3C1C1A01086408) funded by the Korean National Research Fund.

Byungjin Lee is with the Academy of Applied Science and Technology, Konkuk University, Seoul 05029, Korea (e-mail: schumir@konkuk.ac.kr). Juhwan Lee is with the Department of Aerospace Information Engineering, Konkuk University, Seoul 05029, Korea (e-mail: lmkknjjb@naver.com). Sangkyung Sung is with the Department of Mechanical and Aerospace Engineering, Konkuk University, Seoul 05029, Korea (e-mail: sksung@konkuk.ac.kr).
* Corresponding author.

a coil to compensate the weak signal strength, the coverage can be extended wider, but it gives rise to too much strong signal strength which can't be measured by a sensor when it is placed near the coil. The blind zone near the coil cuts down on the available area for positioning.

To overcome this shortage, the size of the coil can be one of the solutions. A circular coil with large diameter reduces the magnetic flux density at a center of the coil and spreads the magnetic field further. The magnetic field model by a circular coil is derived from its geometric relation and Biot-Savart Law. In medical field, this circular current loop model has been well known for developing diagnostic instruments like MRI [5-8].

In the field of biomedical robotics, the circular coil is also applied for the micro-size robot control, where the magnetic field is generated by the circular coil for controlling micro-size magnetic robots. However, elliptic integrals in the circular current loop model necessitate long computation time of the numerical integration. Because of this disadvantage, biomedical robotics area adopts another model for describing the magnetic field, which is the magnetic dipole model. This dipole model assuming a sphere shape magnet has a simple equation form and an advantage of short computation time. Even though several studies suggest the availability of the circular current loop model by the enhanced numerical method for the elliptic integrals [9,10], many studies still apply the magnetic dipole model because of the above benefits [11-13].

In the field of navigation and positioning, the artificial magnetic field generated by a circular coil has been studied for large area positioning (> 1 m). In this case too, the magnetic field is described as the dipole model in many studies [14-18]. There is a recognition about the enhanced accuracy of positioning by the circular current loop model, but it also values the short computation time of the dipole model [19]. The dipole model is an efficient way to describe the magnetic field when the radius of a circular coil is small enough. Or, if a signal receiver doesn't approach the coil closely, the small coil assumption can be validated even though a large coil is used. Many research cases assume this environment where the motion of a signal receiver is blocked by some object for approaching a coil, or the receiver keeps a proper distance from the coil. In these cases, the advantage of the dipole model can be valid generally for many applications in various fields. When the above constrains are not available, however, the dipole model has non-negligible error near a coil. Even though the 'dead zone' is removed by adopting the large coil, this area is still unavailable for the pose estimation by the dipole model. To overcome this, more complicated but computationally comparable formula is investigated, which can reflect effectively the dimensional field distribution characteristics of the magnetic coil including near-field area from transmitter.

The motivation and the contributions of this study are as follows: First, comprehensive comparison on magnetic models for pose estimation is provided including conventional models and a newly proposed coil-based model. To validate the performance, experimental error analysis from various models are presented along with mathematical representation formula. Specifically, four circular coils with a meter-sized diameter are fabricated to generate the AC magnetic fields, and the operational test with the expanded coil coverage is done to analyze the estimation performance. High precision electronics with a low offset and temperature drift is implemented to mitigate measurement uncertainty effect. Besides, environmental interference is best approximated in the suggested coil model through analyzing error distribution from static experiments. As a result, considering the ratio of the coil diameter and the operational range, this study demonstrates that the pose estimation results are superior to other methods in the field of magnetic positioning technology, to the best of author's knowledge. Second, the feasibility of the suggested algorithm is verified through an on-board microprocessor in a real time manner. As small coil sizes are assumed, many existing studies have adopted the conventional dipole model because of computational efficiency. This study empirically provides the experimental proof of the computational feasibility of the circular current loop model. The employed model is composed only of constant polynomials and their multiplications, which is advantageous in a microprocessor platform. As a result, the pose estimation results are achieved through an uncomplicated numerical optimization algorithm in the microprocessor for its on-board implementation. Third, the performance of the proposed algorithm is demonstrated via mission trajectory experiments using embedded computer onboard the UGV (unmanned ground vehicle). For a quantitative analysis on the estimation result, a reference data is measured through an optical motion tracking system. Two representative cases are introduced in experiments, where enhanced estimation accuracy is secured by the proposed field model even in real-time environment. It is observed that the resulting estimation error ranges within 1% of effective coverage for both static and dynamic tests.

The structure of the paper is as follows: Section 2 presents the basic principle of the magnetic field navigation system under consideration. The proposed magnetic field models and other benchmark models are presented in Section 3, followed by the performance comparison through static experiments in Section 4. Section 5 demonstrates the performance of the proposed method through indoor dynamic experiments, and finally, it is summarized conclusion in Section 6.

2. BACKGROUND METHODS

2.1. Signal and data processing

The MPS (magnetic positioning system) in this study consists of two parts: a receiver and transmitters. The fundamental of the system is already introduced in author's previous study [22].

Thus, only brief description is given in this literature. First, multiple transmitters generate the magnetic fields which are superposed with different carrier frequencies. Each transmitter has its controller, a coil and capacitor array. The role of the controller is to convert the input voltage V_s to the controlled voltage V_c, and to drive the LC resonance circuit by two PWM signals with opposite phases. The AC magnetic field from a circular coil is approximated by each representation model, which is illustrated in detail in the next section. Given the coil's inductance with physical dimensions, the resonance frequency can be tuned by the capacitance of the capacitor array which is composed of small capacitors. Each frequency of the LC circuit is designed as 500, 600, 700 and 800 Hz, respectively. Fig. 1 depicts the four coils and the role of the transmitter controller.

The receiver measures the superposed AC magnetic signal by 3-axis magnetometer. The measured signal is processed by analog circuits before AD converting. Each axis signal is amplified and filtered two times through the circuits. The band pass filter is composed of a −40 dB LPF (low pass filter) and HPF (high pass filter) for removing DC signal and high frequency noise. Together with a micro-processor, the sensor and the analog circuit are both placed on the receiver board. Fig. 2 depicts the conceptual block diagram with the 3-axis magnetometer and the functional analog circuits.

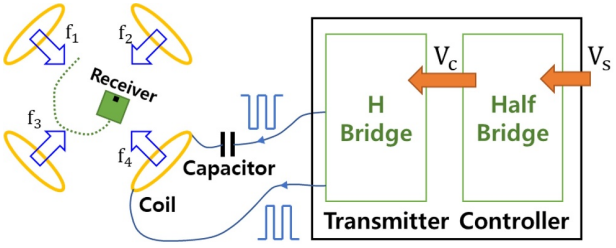

Fig. 1. AC magnetic field generation.

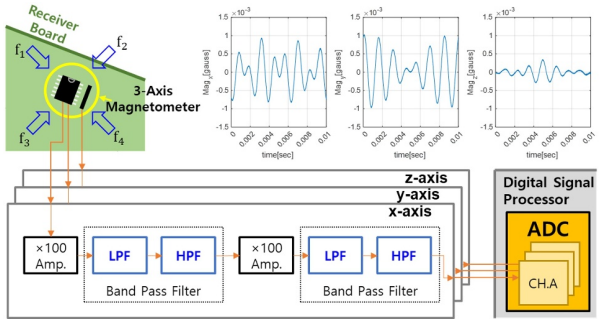

Fig. 2. Receiver electronics and ADC measurement.

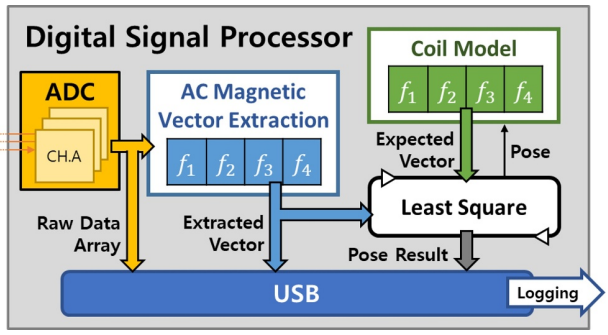

Fig. 3. Algorithm architecture in a micro processor.

The amplified and filtered analog signal is acquired by ADC (analog to digital converter) in a micro-processor (i.e., DSP, digital signal processor). This 16-bit ADC acquires 4000 samples per axis in 0.01 seconds, so the total size of the 3-axis data array is 24000 bytes. The raw data array is sent to a laptop computer via serial communication, and the logged data is utilized to develop algorithms for magnetic vector extraction and pose estimation via the proposed coil model. Specifically, this study includes the real time implementation of the algorithms on the board. Fig. 3 shows the algorithm flow in the micro-processor. From the raw data array, concurrent magnetic field vectors are extracted by each frequency. Meanwhile, the coil model is used to compute each expected magnetic vector. Using these extracted and expected vectors, the numerical optimization algorithm computes the pose (e.g., position and attitude). The pose is used again as input variable to the coil model, and more accurate pose is calculated through the iteration of the numerical process. As the pose estimation is completed with a converged value, a consecutive ADC sampling begins for estimating the next pose.

The fundamentals of AC magnetic vector extraction and the numerical computation process are covered in this section, while the essential representation model is introduced in Section 3.

2.2. AC magnetic vector extraction

The magnetic vector extraction is essential for realtime implementation. For explanation of the algorithm, consider first the superposed magnetic signal model described as

$$\boldsymbol{M} \equiv \begin{bmatrix} M_x \\ M_y \\ M_z \end{bmatrix} = \sum_{i=1}^{4} \left\{ \begin{bmatrix} m_i \cdot \sin(\omega_i \cdot t + \alpha_i) \\ n_i \cdot \sin(\omega_i \cdot t + \beta_i) \\ l_i \cdot \sin(\omega_i \cdot t + \gamma_i) \end{bmatrix} + \boldsymbol{B}_i \right\}. \tag{1}$$

Here $\boldsymbol{M}$ means the 3-axis data array acquired in the DSP after passing through analog electronics. Each frequency (f_i, $i = 1, 2, 3, 4$) signal has the angular frequency ω_i

$(= 2\pi \cdot f_i)$ and 3-axis phases α_i, β_i, γ_i, respectively. Each magnetic field vector has three amplitudes m_i, n_i, l_i, which are measured by the 3-axis magnetometer. The four AC signals are superposed on $\boldsymbol{M}$.

In (1), $\boldsymbol{B}_i$ represents remaining bias term that may originate from implementation errors in electronics such as amplifier, filter or ADC. In practice, the geomagnetic field is negligible in $\boldsymbol{B}_i$ as the bandpass filter sufficiently suppresses the DC magnetic component as compared with the artificially generated signals in the carrier frequency band. For an enhanced estimation result, however, the remaining bias term should be further eliminated, which is achieved through the following magnetic vector demodulation process. Equation (2) shows two reference sinusoidal values for the vector extraction of the i-th AC field. The reference values have same frequencies with the i-th field, and the phases $\theta_{1,i}$ and $\theta_{2,i}$ are temporary values to explain the extraction from (3) to (6).

$$\begin{aligned} r_{1,i} &= \sin(\omega_i \cdot t + \theta_{1,i}), \\ r_{2,i} &= \sin(\omega_i \cdot t + \theta_{2,i}). \end{aligned} \tag{2}$$

In (3), the one axis data M_x is multiplied by the reference sinusoidal signals and integrated with time. The derivation results of the integration can be simplified like the right sides of (3), because the ADC sampling time Δt is 0.01 seconds and the four frequencies (500-800 Hz) are integer multiples of '$1/\Delta t\ (= 100)$'.

$$\begin{bmatrix} \int_t^{t+\Delta t} M_x \cdot r_{1,i} dt \\ \int_t^{t+\Delta t} M_x \cdot r_{2,i} dt \end{bmatrix} = \frac{\Delta t}{2} \cdot m_i \cdot \begin{bmatrix} \cos(\alpha_i - \theta_{1,i}) \\ \cos(\alpha_i - \theta_{2,i}) \end{bmatrix}. \tag{3}$$

Meanwhile, the left sides of (3) are calculated by numerical integrations. The equations are summarized as (4) using temporary values y_1 and y_2.

$$\begin{bmatrix} y_1 \\ y_2 \end{bmatrix} = m_i \cdot \begin{bmatrix} \cos\theta_{1,i} \cdot \cos\alpha_i + \sin\theta_{1,i} \cdot \sin\alpha_i \\ \cos\theta_{2,i} \cdot \cos\alpha_i + \sin\theta_{2,i} \cdot \sin\alpha_i \end{bmatrix}, \tag{4}$$

where

$$\begin{bmatrix} y_1 \\ y_2 \end{bmatrix} \equiv \frac{2}{\Delta t} \cdot \begin{bmatrix} \int_t^{t+\Delta t} M_x \cdot r_{1,i} dt & \int_t^{t+\Delta t} M_x \cdot r_{2,i} dt \end{bmatrix}^T.$$

Equation (5), a factorizing equation of (4), has a 2×2 matrix. If $\theta_{2,i}$ is set as 90 degrees and $\theta_{1,i}$ is zero, the matrix becomes an identity matrix as (6).

$$\begin{bmatrix} y_1 \\ y_2 \end{bmatrix} = m_i \cdot \begin{bmatrix} \cos\theta_{1,i} & \sin\theta_{1,i} \\ \cos\theta_{2,i} & \sin\theta_{2,i} \end{bmatrix} \cdot \begin{bmatrix} \cos\alpha_i \\ \sin\alpha_i \end{bmatrix}, \tag{5}$$

$$\begin{bmatrix} y_1 \\ y_2 \end{bmatrix} = m_i \cdot \begin{bmatrix} \cos\alpha_i \\ \sin\alpha_i \end{bmatrix}. \tag{6}$$

Consequently, the amplitude and phase are computed by (7) and (8).

$$m_i = \sqrt{{y_1}^2 + {y_2}^2}, \tag{7}$$

$$\tan\alpha_i = \frac{y_2}{y_1}. \tag{8}$$

Other axes data $(n_i,\ l_i)$ can be extracted in the same way. If a phase is 180 degrees different from other phases, the axis value has a negative value with the same amplitude. Finally, each process is repeated for obtaining four AC magnetic field vectors $\boldsymbol{M}_i = [m_i\ \ n_i\ \ l_i]^{\mathrm{T}}$.

2.3. Numerical pose computation

This study adopts a typical least square algorithm to estimate the pose results. As the basic algorithm is well introduced, the detailed explanation is omitted, and the estimating states and the observation model in the magnetic positioning case are only focused in this paper.

The states $\boldsymbol{x}$ defined in (9) is composed of planar position $\boldsymbol{p}_n$ and heading ψ of the receiver. The subscript n means N-frame (navigation frame) for expressing the pose information.

$$\boldsymbol{x} \triangleq \begin{bmatrix} \boldsymbol{p}_n \\ \psi \end{bmatrix} = \begin{bmatrix} p_x \\ p_y \\ \psi \end{bmatrix}. \tag{9}$$

Equation (10) defines a direction cosine matrix (DCM) in terms of the heading ψ.

$$\mathbf{C}_n^b(\psi) = \begin{bmatrix} \cos\psi & \sin\psi & 0 \\ -\sin\psi & \cos\psi & 0 \\ 0 & 0 & 1 \end{bmatrix}. \tag{10}$$

As the 3-axis magnetometer is fixed on the receiver board, the magnetic vectors are measured in a B-frame (i.e., body frame). Meanwhile, because the coil model, which is introduced in the next section, provides the theoretical magnetic vectors $\boldsymbol{B}_i^n$ in N-frame, the observation model represented in the B-frame requires a frame transformation using DCM $\mathbf{C}_n^b$ as in (11). Then the propagated magnetic vector represented in the body frame, $\boldsymbol{B}_i^b$ is arranged by

$$\boldsymbol{B}_i^b \equiv \begin{bmatrix} \boldsymbol{\mu}_i \\ \eta_i \end{bmatrix}_{3\times1} = \mathbf{C}_n^b \cdot \boldsymbol{B}_i^n, \tag{11}$$

where $\boldsymbol{\mu}_i$ is the planar position vector and η_i is elevation. Here note that $\mathbf{C}_n^b$ is related with the attitude expression via ψ, thus the coil model is represented through the states $\boldsymbol{x}$. Thus the observation model with the truncated position vector is newly defined by

$$h_R(\boldsymbol{x}) = \begin{bmatrix} \boldsymbol{\mu}_1 \\ \boldsymbol{\mu}_2 \\ \vdots \end{bmatrix}. \tag{12}$$

In our study, a linear approximation approach is employed to obtain the optimal pose estimate. The Jacobian matrix of $h(\boldsymbol{x})$ with respect to pose states $\boldsymbol{x}$ is given as

$$\boldsymbol{H}_R = \left[\frac{\partial h_R(\boldsymbol{x})}{\partial \boldsymbol{x}} \right]_{2i\times3}. \tag{13}$$

In (13), it is observed $2i$ by 3 Jacobian elements are adapted in the planar pose estimation problem, yet the linearized model can be augmented if the state variables extend to include the elevation in position and horizontal angles of roll and pitch. In the planar pose estimation problem, the observation model is simply reduced to contain state variable of horizontal motion. Given the linearized model, a typical least square estimation is employed as shown below.

$$\begin{bmatrix} \widetilde{\boldsymbol{p}}_n \\ \widetilde{\psi} \end{bmatrix} = \left(\boldsymbol{H}_R^{\mathrm{T}} \cdot \boldsymbol{H}_R\right)^{-1} \cdot \boldsymbol{H}_R^{\mathrm{T}} \cdot \left(\begin{bmatrix} \vdots \\ \boldsymbol{M}_i\,(1:2) \\ \vdots \end{bmatrix} - \begin{bmatrix} \vdots \\ \boldsymbol{\mu}_i \\ \vdots \end{bmatrix} \right). \tag{14}$$

In (14), stacked residuals between the reduced measurement vector of $\boldsymbol{M}_i$ and the model-based vectors $\boldsymbol{\mu}_i$ are used for computing estimate update. In (15) and (16), the estimated error is compensated in the pose $\widehat{\boldsymbol{p}}_{n,k}$ and $\widehat{\psi}_k$. k is the number of the iteration for the least square. When the iteration error gets lower than a nominal threshold, the process is finished, and the pose is finally determined.

$$\widehat{\boldsymbol{p}}_{n,k+1} = \widehat{\boldsymbol{p}}_{n,k} + \widetilde{\boldsymbol{p}}_n, \tag{15}$$

$$\widehat{\psi}_{k+1} = \widehat{\psi}_k + \widetilde{\psi}. \tag{16}$$

3. MAGNETIC FIELD MODEL

3.1. Coil geometry and coordinate system

In this section, magnetic coil geometry and parameters are illustrated for further analysis. As pose estimation through magnetic source requires a strong magnetic intensity in a spatially expanded coverage, coil with sufficient dimension and windings is designed. The radius of the circular coil is denoted a and the current is I in this study. For expressing the coil model, another frame is defined in this section. That is C-frame (coil frame). The origin point of this frame is the center of the coil, and the x-axis is defined as the center axis in Fig. 4. The y-axis of C-frame can have any directions orthogonally to the x-axis, because of the axisymmetric shape of the circular coil. In this study, the

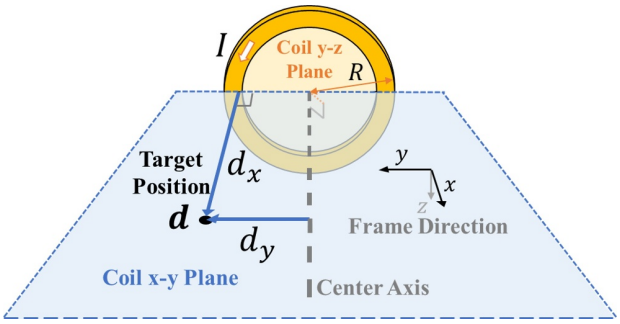

Fig. 4. Circular coil geometry.

y-axis is defined by the definition of the z-axis as the gravitational direction. The coil x-y plane includes the x and y axis, and the target $\boldsymbol{d}$ ($\equiv \begin{bmatrix} d_x & d_y & 0 \end{bmatrix}^{\mathrm{T}}$) is defined on this plane.

The coil also has its pose (position and attitude) in N-frame. The receiver position $\boldsymbol{p}_n$ is converted to the target position $\boldsymbol{d}$ as (17). The coil position is denoted as $\boldsymbol{p}_{\mathrm{coil},n}$ in N-frame and the DCM $\mathbf{C}_n^c$ rotates the vector from N-frame to C-frame.

$$\boldsymbol{d} = \mathbf{C}_n^c \cdot \left(\boldsymbol{p}_n - \boldsymbol{p}_{\mathrm{coil},n}\right). \tag{17}$$

Equation (18) shows the generalized magnetic field vector equation. By the coil model, the estimated vector $\boldsymbol{B}^c$ is computed with the input variable $\boldsymbol{d}$ in C-frame, and the C-frame is converted to N-frame by the DCM $\mathbf{C}_c^n$. The result $\boldsymbol{B}^n$ represents the magnetic field vector in N-frame.

$$\boldsymbol{B}^n = \mathbf{C}_c^n \cdot \boldsymbol{B}^c. \tag{18}$$

This study adopts the four coils, and they are place on their different poses. Applying the coil parameters to the generalized coil model equation in (18), vectors $\boldsymbol{B}_i^n$ from the i-th coil are finally computed for the observation model in (11).

3.2. Dipole model

For the comparison with the circular current loop model, this study introduces a dipole model that is widely adopted in previous studies [14-18]. The dipole model assumes that a sphere shape magnet has two magnetic poles. This assumption is not appropriate to the circular coil, but the field estimation is relatively accurate when the receiver keeps the distance from the coil ($d \gg R$). A typical magnetic flux density of dipole model is depicted as follows:

$$\boldsymbol{B}_{c,\mathrm{dipole}}(\boldsymbol{d}) = \gamma_{\mathrm{dipole}} \cdot \left(\frac{3\boldsymbol{d} \cdot (\widehat{\boldsymbol{n}} \cdot \boldsymbol{d})}{d^5} - \frac{\widehat{\boldsymbol{n}}}{d^3} \right), \tag{19}$$

where

$$\gamma_{\mathrm{dipole}} = \frac{\mu_0 \cdot N \cdot I \cdot R^2}{4},\ d = \|\boldsymbol{d}\|.$$

Note that $\widehat{\boldsymbol{n}}$ is the center axis direction of the coil, which has always $\begin{bmatrix} 1 & 0 & 0 \end{bmatrix}^{\mathrm{T}}$ in the C-frame. μ_0 is the magnetic permeability of free space, and its value is given as $4\pi \times 10^{-7}\mathrm{H/m}$. The number of turns N is an integer coefficient. Other notations are the same as the circular current loop model.

3.3. Circular coil model

The circular current loop model (shortly 'circular model') is basically derived from the Biot-Savart law. The derivation process is complicated with mathematical principals and developments, and is introduced in detail for the navigation and positioning purpose in [22]. By omitting

the details of the derivation, the only resulting equations are arranged as below.

$$\boldsymbol{B}_{c,\text{circle}}(\boldsymbol{d}) = \begin{bmatrix} \frac{\gamma_{\text{circle}}}{\sqrt{s_1}} \cdot \left(\frac{e_1}{s_2} \cdot E(k) + K(k) \right) \\ \frac{\gamma_{\text{circle}} \cdot x_c}{y_c \cdot \sqrt{s_1}} \cdot \left(\frac{e_3}{s_2} \cdot E(k) - K(k) \right) \\ 0 \end{bmatrix}, \tag{20}$$

where

$$\gamma_{\text{circle}} = \frac{\mu_0 \cdot N \cdot I}{2\pi}, \qquad e_1 = R^2 - {d_x}^2 - {d_y}^2,$$
$$s_1 = {d_x}^2 + (d_y + R)^2, \qquad e_2 = R^2 + {d_x}^2 - {d_y}^2,$$
$$s_2 = {d_x}^2 + (d_y - R)^2, \qquad e_3 = R^2 + {d_x}^2 + {d_y}^2.$$

In (20), $K(k)$ and $E(k)$ are the elliptic integral of the first and second kinds, and their incomplete forms are described as

$$K(k) = \int_0^{\pi/2} \left(\frac{1}{(1 - k^2 \cdot \sin^2\phi)^{\frac{1}{2}}} \right) d\phi,$$
$$E(k) = \int_0^{\pi/2} \left((1 - k^2 \cdot \sin^2\phi)^{\frac{1}{2}} \right) d\phi, \tag{21}$$

where

$$k^2 = \frac{4R \cdot d_y}{s_1}.$$

The above coil equations can be used for the magnetic positioning by applying the numerical integration of (21). Because of the computational efficiency, however, the complete forms are usually adopted as the integral equations. In this study, two types of the complete forms are compared. The first ones are polynomial approximation method as (22). This method has advantages about the finite number of the polynomials and small error ($< 2.0 \times 10^{-8}$). The coefficients of the polynomials ($a_{0\sim4}$, $b_{0\sim4}$, $c_{1\sim4}$, $d_{1\sim4}$) are well introduced in other studies (Hastings, 1955, Sheet: 47, 51) [19-21], so they are not denoted in this paper.

$$K_A(k) = \sum_{i=0}^{4} \left(a_i \cdot {k_1}^i \right) + \left(\sum_{i=0}^{4} \left(b_i \cdot {k_1}^i \right) \right) \ln \frac{1}{k_1},$$
$$E_A(k) = 1 + \sum_{i=1}^{4} \left(c_i \cdot {k_1}^i \right) + \left(\sum_{i=1}^{4} \left(d_i \cdot {k_1}^i \right) \right) \ln \frac{1}{k_1}, \tag{22}$$

where

$$k_1 = 1 - k^2.$$

Compared with (22) that includes the logarithm operations, Legendre polynomial method only consists of the polynomial multiplications as (23) [9,21]. In this study, we newly propose an integration algorithm based on the finite number of Legendre polynomial model for describing the circular model in (20). Note that the equation can obtain true solution if infinite summation of polynomials is computed in (23). However, the summation number n can provide a trade-off between the accuracy and the computation time. Thus a compromise between performances can be figured out as a design factor.

$$K(k) = \frac{\pi}{2} \cdot \left[1 + \sum_{i=1}^{n \to \infty} \left(\frac{(2i-1)!!}{(2i)!!} \cdot k^i \right)^2 \right],$$
$$E(k) = \frac{\pi}{2} \cdot \left[1 - \sum_{i=1}^{n \to \infty} \left(\frac{(2i-1)!!}{(2i)!!} \cdot k^i \right)^2 \cdot \frac{1}{2i-1} \right]. \tag{23}$$

4. STATIC ERROR ANALYSIS

4.1. Transmitter and receiver design

The hardware of the transmitter and receiver are is implemented as in Fig. 5. The bridges of the transmitter are composed with 750 V/12 A NPN transistor ST1510FX, and the control signal is generated by Cortex M3 microprocessor STM32F103x. The half bridge controls V_C to 1.25 V with V_S (= 5 V) depicted in Fig. 1. The LC resonance circuit is driven by the H-Bridge drives, and the resonance frequency is tuned by the capacitor array. The coil diameter is 1.005 m, and its inductance is 96-97 mH. Fig. 5 shows the detailed electronics of TX controller. The 3-axis magnetometer in the receiver module consists of 1 and 2-axis magnetometer HMC 1001, 1002.

Each axis signal is amplified and filtered through the analog circuit with LT1114 op-amps. The analog circuit has 13 op-amp boards, and each board can be replaced for circuit configuration. The analog signals are converted by ADC modules in the micro-processor TMS320F28388D. As a featured hardware implementation, DSP was employed in RX side for high-speed data processing of con-

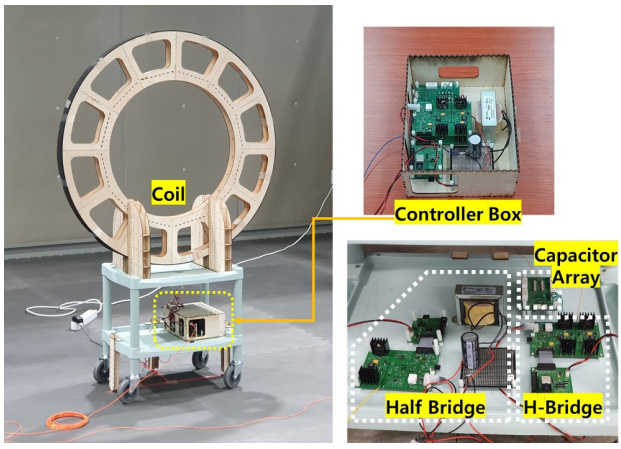

Fig. 5. Manufactured coil and control electronics for AC magnetic transmitter.

current magnetometer signals and real-time algorithm performance. In TX side, the Cortex M3 processor was used for carrier frequency signal generation, which requires relatively low computational power and capacity. Also, measurement uncertainty is significantly mitigated by employing the qualified electronic components including very low offset op-amps, drift-free passive components, and high-precision magnetometer.

4.2. Static experiment environment and result

For validating the proposed reduced-order polynomial model and evaluating the pose estimation performance, static experiment using grid map data is done before real-time dynamic experiment. A comparative estimation error analysis of each model helps to select superior model that can best suppresses the magnetic interference and environmental noises present in the test facility.

In static tests, the grid interval is 0.6 m, and there are 81 (9×9) points on the floor as shown in Fig. 6. The distance between two opposite coils is 6.0 m. The marker in the floor depict respectively the grid point at the line intersection. Note that there exists a tradeoff between complexity and accuracy according to the coil number and deploying shape. In this study, a typical configuration with four TX coils in a square installation is established as in Fig. 6, which representatively provides the characteristic estimation performance. The receiver saves the data for 15 seconds at every grid point. The ADC sampling is operated every 0.1 second in the receiver, thus 150 raw data arrays are acquired at each grid point. In analyzing the static experimental results, the raw data arrays are analyzed via post-processing using the Matlab on a PC and the precise reference data at each grid is obtained by the OptiTrack system.

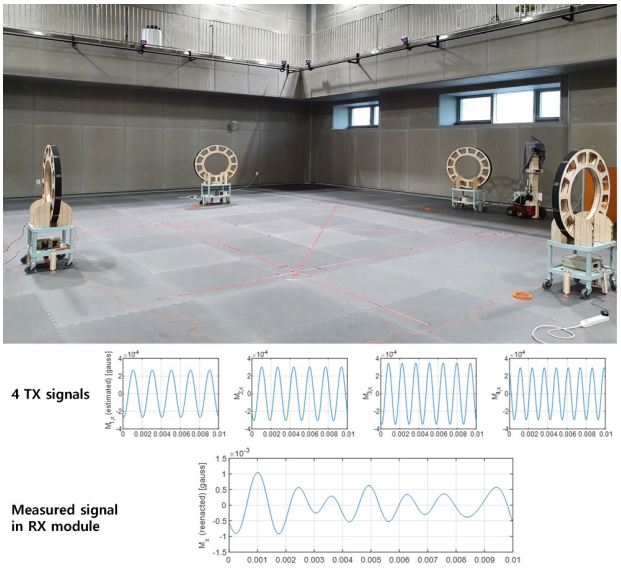

Fig. 6. Environment of static performance experiment.

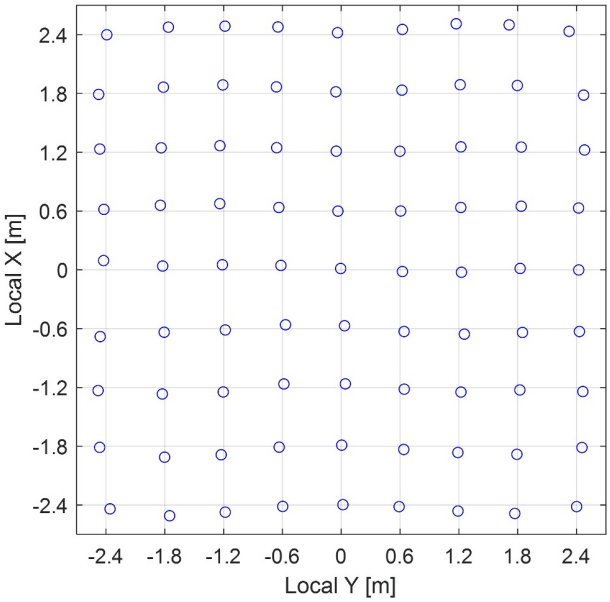

Fig. 7. Grid positioning result of Legendre $\{n = 1000\}$.

The purpose of this analysis is to compare the error performance of the three coil models; i.e., dipole model, circular model with polynomial approximation (shortly 'Approx.') and two Legendre polynomial models (shortly 'Legendre $\{n\}$'). Here, 'n' implies the Legendre polynomial order. This study assumes that Legendre $\{n = 1000\}$ provides a true circular coil model, which is presented in Fig. 7. The intersection of the grids in the graph are depicted to analyze performance at each points, and blue circle markers are the positioning results though the least square with Legendre $\{n = 1000\}$. An averaged vector of the 150 vectors at each point are used for the positioning. Although it is observed there are some off-grid points in the grid map, most estimate points locates near nominal grid points.

Fig. 8 depicts contour graphs of the positioning error. For each model, the error is calculated using reference position acquired from the OptiTrack system. First, Fig. 8(a) is the error contour results in Fig. 7. First, the error of the dipole model in Fig. 8(b) shows slightly better results than Fig. 8(a) and Fig. 8(c) around the central region. Although they provided more accurate result at partial region, overall performance is inferior to the circular coil model because of a drastic degradation near coil proximity region. In static experiment, the closest distance between the grid points and the coils is 0.6 m. Considering the diameter of the coil, this near-field region is not sufficiently separated from the coils, which fails to yield effectiveness of the dipole model.

Noted as an advantage of the Approx. method, Fig. 8(c) is similar to Fig. 8(a) and shows a proper error distribution without significant deterioration. Furthermore, it can be

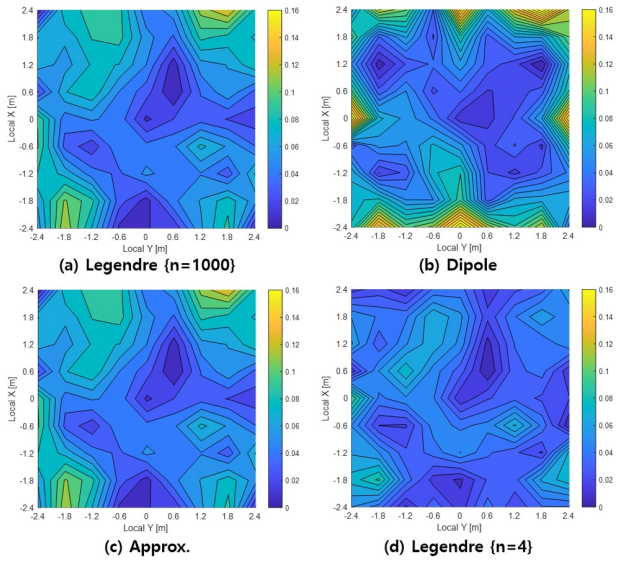

Fig. 8. Error results of the grid data.

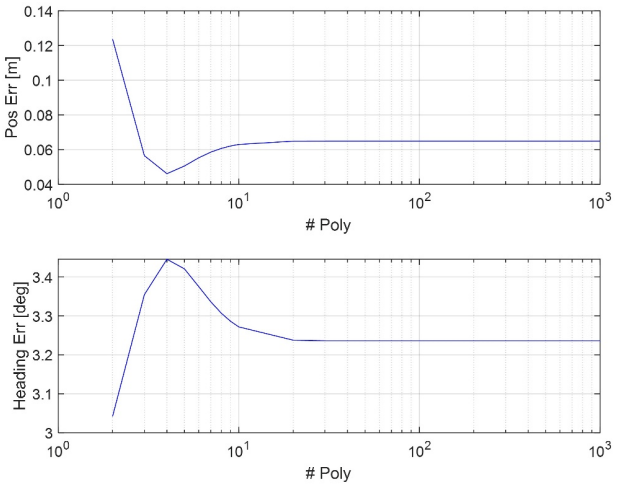

Fig. 9. Error characteristics according to the Legendre polynomial orders.

observed that, although the Legendre $\{n = 1000\}$ model best represents true mathematical circular coil model, the Legendre $\{n = 4\}$ model in Fig. 8(d) shows rather superior error performance compared with other methods. Fig. 9 shows the comprehensive comparison of the estimation performance according to the approximation degree of the Legendre polynomial using the data from an experimental environment with measurement interference. In the figure, the estimation errors of position and heading is displayed according to the degree of Legendre polynomial, which confirms that the minimum position error was obtained with $\{n = 4\}$ model.

Deviation from theoretic model is essentially due to the environmental magnetic interferences which mainly originate from the induced eddy currents through the building structure containing ferromagnetic materials. Thus, it is confirmed that, given environmental interferences, static error analysis can provide more proper approximation model than a pure theoretic model that fails to reflect the practical magnetic field anomaly.

Table 1. The average error of the static experiment.

	Positioning error	Heading error
Legendre $\{n = 1000\}$	5.86 cm	3.24°
Approx.	5.86 cm	3.24°
Dipole	6.61 cm	3.54°
Legendre $\{n = 4\}$	4.18 cm	3.45°

In summary, Table 1 compares overall static estimation error results including the order of the Legendre polynomials and other comparative methods. In Table 1, position error and heading error are computed as follows, respectively:

$$\varepsilon_{\boldsymbol{p}} = \frac{1}{M} \cdot \sum_{i_t=1}^{M} \left\| \boldsymbol{p}_n(i_t) - \boldsymbol{p}_{n,\mathrm{ref}}(i_t) \right\|, \tag{24}$$

$$\varepsilon_{\psi} = \frac{1}{M} \cdot \sum_{i_t=1}^{M} \{ |\psi(i_t) - \psi_{\mathrm{ref}}(i_t)| \}, \tag{25}$$

where $\boldsymbol{p}_{n,\mathrm{ref}}$ and ψ_{ref} represents position and heading from reference sensor, respectively. M is the number of time epochs. The table concludes that $\{n = 4\}$ is the best result for the positioning. Note that the heading error is slightly higher at $\{n = 4\}$, which is negligible as 0.2°.

5. DYNAMIC EXPERIMENT AND ANALYSIS

5.1. Experimental configuration

Dynamic experiments is done using the MPS receiver onboard UGV platform in the indoor test facility. The UGV cart operates with four independent motors, which is controlled by remote controller manually. The received data from the receiver is saved in a laptop computer. The dynamic performance of the pose estimation is evaluated by an independent optical method, i.e., the OptiTrack system with 16 prime$^{\times}$13 cameras. Through calibration process of the system, it provides sub-millimeter accuracy position data of the optical markers. Pictures in Fig. 10 show the experimental environment, including the UGV, embedded sensor module, transmitter coils, and tracking camera system.

Fig. 11 depicts the overall algorithm and data flow in the DSP processor. In the figure, the adopted micro-processor includes three independent cores, which are named CPU1, CPU2 and CM (connectivity manager). CPU1 controls the 16-bit ADC modules to convert the analog signals to 3×4000 raw data array for 0.01 seconds. The data array is shared with other cores through IPC (inter processor communication). The main algorithm for the pose estima-

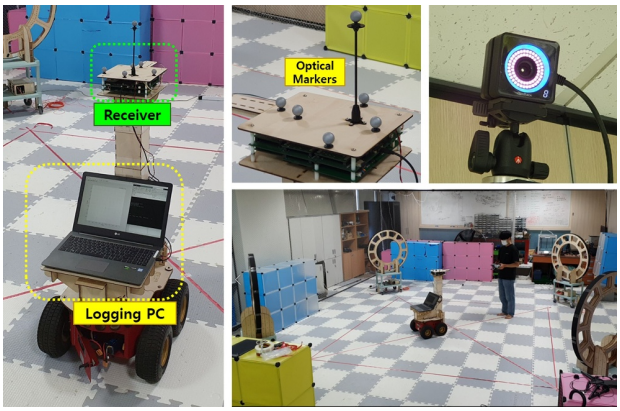

Fig. 10. Real time experiment environment.

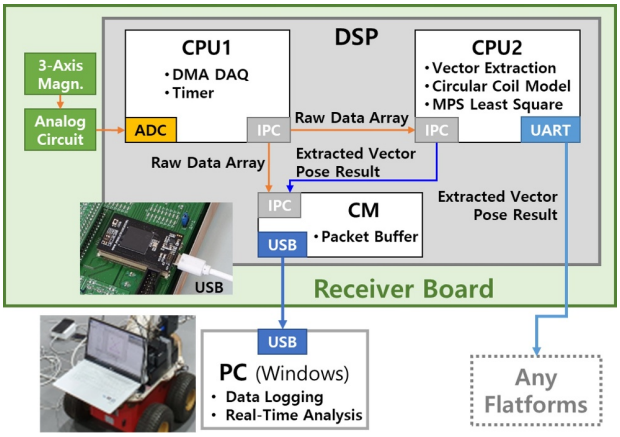

Fig. 11. Onboard realtime platform and emulator structure for performance comparison.

tion is operated in CPU2. The results of the vector extraction and pose estimation are transferred to the connected platform through UART interface for robot applications or other purposes. The CM collects the raw data array and the estimation results, and makes USB packet for logging the data. Because of the memory limitation of the DSP, the data is saved at a laptop computer, which is further used in the following performance analysis.

5.2. Real time pose estimation result

In this section, Approx. and Legendre $\{n = 4\}$ results are compared for a real time performance. For fair comparison between the two methods, an emulation mode is developed in the micro-processor that can generate measurement data in a real-time manner. Except CPU2 in Fig. 11, the functions in other cores are modified to receive the logged data from the PC. CM block manages the received USB packet and CPU1 emulates the ADC acquisition sequence and timing. Thus, CPU2 simply operates in the same environment as the real time experiments. Figs. 12 and 13 show the pose estimation results of various comparative methods. The Legendre $\{n = 4\}$ is a real time result computed in the micro-processor during experiment, and the Approx. is a computed result using the emulated data.

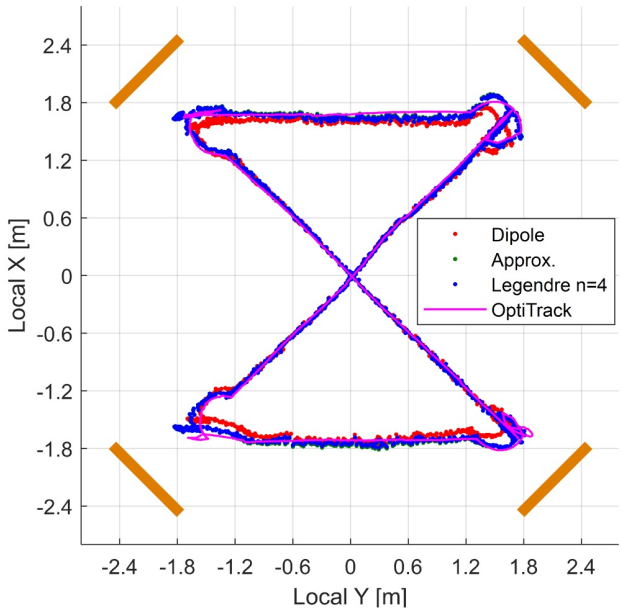

Fig. 12. Pose estimation results of dynamic path.

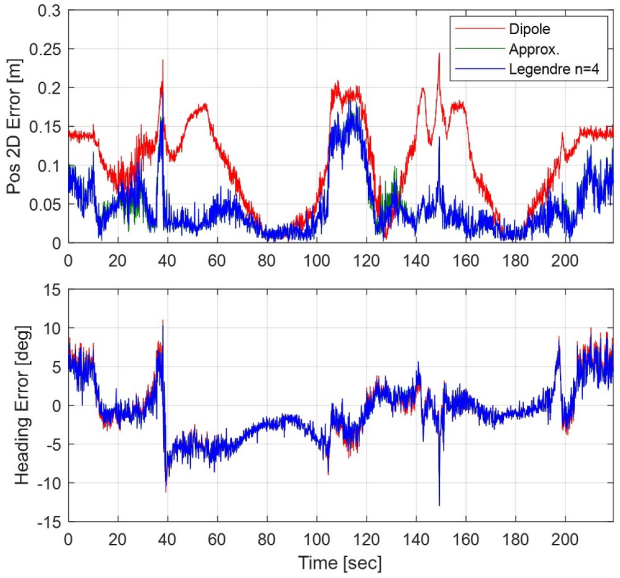

Fig. 13. Error results of dynamic test.

As noted, a typical computing power of a micro-processor is relatively limited compared with a PC or other embedded systems. Not only the clock speed, but also the presence of calculating accelerators makes a big advantageous in a PC environment. A commonly used Intel CPU has MKL (math kernel library) that include many mathematical functions, thus reduces the computing time significantly. Because of the absence of these accelerators, on the contrary, a micro-processor is disadvantageous for the

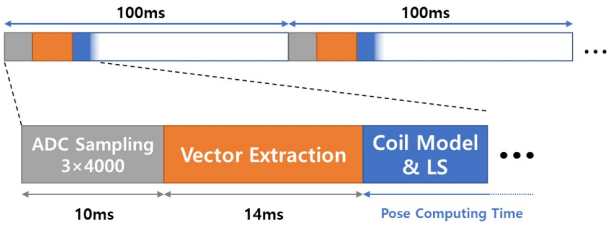

Fig. 14. Timing sequence of ADC and algorithms.

Table 2. The comparison of the real time performance.

	Dipole	Approx.	Legendre $\{n=4\}$
Positioning error	11.58 cm	5.73 cm	5.69 cm
Heading error	3.60°	3.45°	3.45°
Computing time	1.70 ms	2.36 ms	2.34 ms

mathematical operation except simple arithmetic computing.

The employed micro-processor, TMS320F28388D, has a calculating accelerator providing several mathematical functions like __sinpuf32(), __atan2() and __sqrt(). These functions operate without CPU timing consumption, so it is a benefit to implement the proposed system in the microprocessor. The vector extraction, introduced in Section 2, is also implemented with these functions, which takes only 14ms to compute the four 3D vectors even in the microprocessor. The overall timing plan for achieving real-time implementation is described in Fig. 14.

For a comprehensive analysis considering both accuracy and real-time performance, Table 2 provides comparison results of each pose estimation method. Upon examining the results in the table, the proposed method has empirically demonstrated excellent performance in satisfying both accuracy and real-time performance in cases where there are environmental errors and distortions in the magnetic field measurements. Especially, it was experimentally verified that the proposed method can achieve an expanded navigation region compared to a simple dipole model (with good real-time performance due to the model simplicity) while securing the same computational efficiency. Therefore, it can be concluded that the high applicability of the proposed method serves as a essential contribution factor, which demonstrates feasibility for practical navigation application.

6. CONCLUSION

This study suggests the validity of the circular model for the pose estimation in the wide indoor area. The results are different from the conventional conclusions that the dipole model has more advantages than the circular model because of the computation time and its acceptable error. In this study, however, the computation time of the circular model is also reasonable for an indoor application, and this model estimates more accurate magnetic field vector than the dipole model near the coils.

The existing studies accept the small coil assumption of the dipole model. But, when the coil is not small or the distance from the coil is not far enough, the dipole model causes a failure of the positioning, and it can be a potential risk for the complicated application like a robot. This study suggests that the circular model can replace the dipole model even in a micro-processor environment. It can be expected the proposed method applies for positioning and enhances the availability of various applications, especially for real time systems.

CONFLICT OF INTEREST

The authors declare that there is no competing financial interest or personal relationship that could have appeared to influence the work reported in this paper.

REFERENCES

[1] P. R. Slawinski, A. Z. Taddese, K. B. Musto, K L. Obstein, and P Valdastri, "Autonomous retroflexion of a magnetic flexible endoscope," *IEEE Robotics and Automation Letters*, vol. 2, no. 3, pp. 1352-1359, 2017.

[2] S. L. Charreyron, E. Gabbi, Q. Boehler, M. Becker, and B. J. Nelson, "A magnetically steered endolaser probe for automated panretinal photocoagulation," *IEEE Robotics and Automation Letters*, vol. 4, no. 2, pp. 17-23, 2018.

[3] F. Santoni, A. D. Angelis, A. Moschitta, and P. Carbone, "MagIK: A hand-tracking magnetic positioning system based on a kinematic model of the hand," *IEEE Transactions on Instrumentation and Measurement*, vol. 70, pp. 1-13, 2021.

[4] J. Garcia, S. Soto, A. Sultana, J. Leclerc, M. Pan, and A. T. Becker, "Underwater robot localization using magnetic induction: Noise modeling and hardware validation," *IEEE Global Oceans 2020: Singapore–US Gulf Coast*, 2020.

[5] B. C. Breneman, J. R. Purcell, and S. C. Burnett, "MRI magnet system having shield and method of manufacture," U.S. Patent No. 4,743,880. 10 May 1988.

[6] L. K. Forbes, S. Crozier and D. M Doddrell, "Rapid computation of static fields produced by thick circular solenoids," *IEEE Transactions on Magnetics*, vol. 33, no. 5, pp. 4405-4410, 1997.

[7] S. Crozier and F. Liu, "Numerical evaluation of the fields induced by body motion in or near high-field MRI scanners," *Progress in Biophysics and Molecular Biology*, vol. 87, no. 2-3, pp. 267-278, 2005.

[8] Z. Liang, "An optimal design of actively shielded MRI superconducting magnet," *IEEE Transactions on Applied Superconductivity*, vol. 29, no. 2, pp. 1-4, 2018.

[9] M. Etiévant, A. Bolopion, S. Régnier, and N. Andreff, "An improved control-oriented modeling of the magnetic field," *Proc. of International Conference on Robotics and Automation (ICRA)*, 2019.

[10] J. Begey, M. Etiévant, J. E. Quispe, A. Bolopion, M. Vedrines, J. Abadie, S. Régnier, N. Andreff, and P. Renaud, "A manipulability criterion for magnetic actuation of miniature swimmers with flexible flagellum," *IEEE Robotics and Automation Letters*, vol. 5, no. 3, pp. 4891-4898, 2020.

[11] M. P. Kummer, J. J. Abbott, B. E. Kratochvil, A. Sengul, and B. J. Nelson, "OctoMag: An electromagnetic system for 5-DOF wireless micromanipulation," *IEEE Transactions on Robotics*, vol. 26, no. 6, pp. 1006-1017, 2010.

[12] D. Wong, E. B. Steager, and V. Kumar, "Independent control of identical magnetic robots in a plane," *IEEE Robotics and Automation Letters*, vol. 1, no. 1, pp. 554-561, 2016.

[13] R. Chen, D. Folio, and A. Ferreira, "Mathematical approach for the design configuration of magnetic system with multiple electromagnets," *Robotics and Autonomous Systems*, vol. 135, no. 103674, 2021.

[14] A. Sheinker, B. Ginzburg, N. Salomonski, L. Frumkis, and B.-Z. Kaplan, "Localization in 2D using beacons of low frequency magnetic field," *IEEE Journal of Selected Topics in Applied Earth Observations and Remote Sensing*, vol. 6, no. 2, pp. 1020-1030, 2012.

[15] V. Pasku, A. D. Angelis, M. Dionigi, G. D. Angelis, A. Moschitta, and P. Carbone, "A positioning system based on low-frequency magnetic fields," *IEEE Transactions on Industrial Electronics*, vol. 63, no. 4, pp. 2457-2468, 2016.

[16] V. Pasku, A. D. Angelis, A. Moschitta, P. Carbone, J. -O. Nilsson, S. Dwivedi, and P. Händel, "A magnetic ranging-aided dead-reckoning positioning system for pedestrian applications," *IEEE Transactions on Instrumentation and Measurement*, vol. 66, no. 5, pp. 953-963, 2017.

[17] V. Pasku, A. D. Angelis, G. D. Angelis, A. Moschitta, and P. Carbone, "Magnetic field analysis for 3-D positioning applications," *IEEE Transactions on Instrumentation and Measurement*, vol. 66, no. 5, pp. 935-943, 2017.

[18] M. Hehn, E. Sippel, C. Carlowitz, and M. Vossiek, "High-accuracy localization and calibration for 5-DOF indoor magnetic positioning systems," *IEEE Transactions on Instrumentation and Measurement*, vol. 68, no. 10, pp. 4135-4145, 2018.

[19] G. D. Angelis, A. D. Angelis, A. Moschitta, and P. Carbone, "Comparison of measurement models for 3D magnetic localization and tracking," *Sensors*, vol. 17, no. 11-2527, 2017.

[20] C. Hastings Jr., *Approximations for Digital Computers*, Princeton University Press, Princeton, New Jersey, 1955.

[21] M. Abramowitz and I. A. Stegun, *Handbook of Mathematical Functions with Formulas, Graphs, and Mathematical Tables*, the United States Department of Commerce, National Bureau of Standards (NBS), December 1972.

[22] B. Lee, S. Sung, "Planar pose estimation system design via explicit spatial representation model of concurrent AC magnetic fields," *IEEE Transactions on Instrumentation and Measurement*, vol. 71, Art no. 8505914, 2022.

Byungjin Lee received his B.S. and Ph.D. degrees in aerospace engineering from Konkuk University, Seoul, Korea, in 2010 and 2017, respectively. He used to work for the Defense Agency for Technology and Quality, Korea. He has been continuing his research as a Research Professor at Konkuk University since 2020. His research interests include development of navigation and control system for unmanned vehicles, and he is currently expanding his area to sensor-level navigation systems.

Juhwan Lee received his B.S. and M.S. degrees in aerospace information engineering from Konkuk University, Seoul, Korea, in 2015 and 2017, respectively, where he is currently pursuing a Ph.D. degree. His research interests include high-spinning objects pose estimation, sensor fusion, navigation and coupled systems, inertial sensors, and sports fusion embedded systems.

Sangkyung Sung received his B.S. and Ph.D. degrees in electrical engineering from Seoul National University, Seoul, Korea, in 1996 and 2003, respectively. He worked for Samsung Electronics Co. Ltd., as a senior engineer before joining Konkuk University. Currently, he is a Professor of the Department of Aerospace Information Engineering at Konkuk University, Seoul, Korea. His research interests include inertial sensor, integrated navigation algorithm, sensor fusion, embedded software, and application to mechatronics and unmanned autonomous systems.